POLITEHNICA UNIVERSITY OF BUCHAREST

Doctoral School of Electronics, Telecommunications and Information Technology

Decision no. ..... from .....

Ph.D. THESIS SUMMARY

Constantin-Cristian DAMIAN

CONTRIBUȚII LA DEZVOLTAREA SENZORILOR SE IMAGINE INTELIGENȚI

CONTRIBUTIONS TO THE DEVELOPEMENT OF COMPUTATIONAL IMAGING SENSORS

THESIS COMMITTEE

President	**Prof. Dr. Ing. Bogdan IONESCU**	**Universitatea Politehnica Bucureşti**
Advisor	**Prof. Dr. Ing. Daniela Colțuc**	**Universitatea Politehnica Bucureşti**
Reviewer	**Prof.dr.ing. Liviu GORAȘ,**	**Universitatea Tehnică "Gh. Asachi", Iași**
Reviewer	**CP II dr.fiz. Florin GAROI,**	**Institutul Național pentru Fizica Laserilor, Plasmei și Radiației**
Reviewer	**Conf.dr.ing. Anamaria RĂDOI,**	**Universitatea Politehnica București**

Bucharest 2021

Abstract

With the development and mass production of spatial light modulators, alternative architectures for optical sensors have gained interest. These fall under the umbrella of computational imaging where the desired signal is not measured directly by sensors but related measurements are taken and the signal is reconstructed from them. With this approach the signal can be reconstructed more with less noise than in the classical approach for certain cases like far-infrared and terahertz imaging. Additionally, with better models of the underlying signal or the sensor architecture further improvements can be made in the accuracy of acquisition.

In this thesis we analyze Hadamard spectroscopy and single pixel imaging architecture. We study the noise reduction advantage of Hadamard spectroscopy (Fellget advantage) both theoretically and experimentally and find that the advantage is mitigated by factors related to with the light sensor. We analyse the noise reduction effect of microscanning and its dependence on the number of previews taken. We develop a model for the formation of the point spread function of a single pixel camera and a method for experimental evaluation. We then apply the method in order to improve the image with deconvoluiton.

Acknowledgements

I would like to thank Prof. Daniela Colțuc for guiding me towards a research career ever since I was a second year undergraduate through my master program, for coordinating me during my doctoral studies and in writing this thesis. She introduced me to the world of signal and image processing and sparked my interest in the domain. Her support, guidance, generosity, patience where invaluable for completing my studies.

I would like to thank Prof. Mihai Datcu for the opportunity of being part of the CEOSpaceTech research group and all my colleagues for working with me. Special thanks to PhD. Mihai Petrovici and PhD. Mihai Crișan for their helpful advice.

The idea for the thesis begun from the ongoing projects at CEOSpaceTech. The research for this thesis has begun under the *THz-Imaging* project conducted by CEOSpaceTech between 2013 and 2015 in colaboration with the National Institute for Laser,Plasma and Radiation Physics (INFLPR) and supported by the Romanian Space Agency, STAR Program. It continued under the *Optical Compressive Sensing Technologies for Space Applications (OCS Tech)* project, ESA ITTAO-8235, in 2016. The experimental prototypes presented in the thesis where created by the team at INFLR and the experiments where conducted in collaboration with them.

Special thanks to my collaborators from INFLPR, PhD. Ioan Apostol, PhD. Victor Damian, PhD. Florin Garoi, PhD. Cristian Udrea, PhD. Tiberius Vasile, PhD. Petre C. Logofătu and physicist Adrian Sima, for their expertise and support.

I would also like to thank my coordination team Prof. Vasile Lăzărescu, Assoc. Prof. Daniela Faur and Lect. Lucian Andrei Perişoară.

Contents

Abstract ii
Acknowledgements iii

1 Introduction **1**
1.1 Thesis objectives 2
1.2 Thesis structure 2

2 Single Pixel Imaging **3**
2.1 Basis Scan 4
2.2 Compressive sensing 4

3 Imaging optics and resolution **6**
3.1 The model of Single Pixel Camera PSF 6
3.2 Our method for the measurement the camera PSF 7
3.2.1 Numerical simulations 8
3.2.2 Experimental results 10
3.3 Deconvolution via CS 11
3.3.1 Experiments with estimated PSF 12

4 Hadamard Spectrometry **13**
4.1 Experimental noise evaluation 14
4.2 Microscanning in Hadamard Spectrometry 16
4.2.1 Numerical experiments 18
4.2.2 Physical experiment 19
4.3 Deconvolution of spectra 20

5 Conlusions **21**
5.1 Original contributions 22
5.2 Published papers 23
5.2.1 Journal papers 23
5.2.2 Conference papers 23
5.2.3 Other papers 24

Bibliography **24**

Chapter 1

Introduction

With the recent advancements of computing technology at our disposal we can create images using sensing technologies that were until recently considered infeasible or extract novel information using existing imaging technology. The discipline that enabled such capablilities is called computational imaging. Within this domain a few paradigms are included such as plenoptic imaging, lensless imaging and single pixel imaging.

Single pixel imaging is a paradigm in computational imaging where a single sensor is employed to capture global measurements of a scene and an algorithm is used to reconstruct the scene digitally. It is closely linked to multiplexed spectroscopy where similar measurements are used to reconstruct a spectrum of light instead of a scene. Due to this link many techniques can be ported between the two domains.

Multiplexed spectroscopy has its roots in Michelson's invention of Fourier spectroscopy [17]. He discovered that the interference pattern of light from a certain source is linked to its spectrum by the Fourier transform. Consequently the pattern could be measured and then the spectrum could be computed using the inverse transform. The same configuration is still used in many far infrared spectrometers, especially in space applications [11, 20].

Over half a century later, Harwit [15] proposed the use of Hadamard transform spectrometers due to their ability to reconstruct the spectrum more accurately than classical methods in conditions where the sensor noise is dominant. He had also shown that the same technique can be applied to reconstruct the image of a scene, constituting one of the early examples of single pixel imaging. The technique developed by Harwit used a series of mechanical masks making the technique unfeasible for large number of pixels.

The development of MOEMS (Micro-Opto-Electro-Mechanical Systems) and its application to spectroscopy in [9] had made high resolution Hadamard spectroscopy feasible. With the further advent of compressive sensing theory the same technology was applied to imaging [22] due to the great reduction in the number of needed measurements. The single-pixel camera became linked to compressive sensing due to its popularization in [10].

1.1 Thesis objectives

In this thesis we analyze Hadamard spectroscopy and single pixel imaging architecture. We study the noise reduction advantage of Hadamard spectroscopy (Fellget advantage) both theoretically and experimentally and find that the advantage is mitigated by factors related to with the light sensor. We analyse the noise reduction effect of microscanning and its dependence on the number of previews taken. We develop a model for the formation of the point spread function of a single pixel camera and a method for experimental evaluation. We then apply the method in order to improve the image with deconvoluiton.

1.2 Thesis structure

The second chapter presents the framework of single pixel imaging. It explains the process of acqusition and the metods for reconstructing the acquired image from measurements. Basis Scan (BS) is presented with its advantages particularly in terms of noise reduction. The theory of Compressive Sensing (CS) is summarised with a focus on the choice of the measurement matrix and the sparsifying transform.

The third chapter focuses on single pixel camera resolution evaluation and improvement. This chapter contains contributions from [5] and [7]. The principle of operation and the theoretical resolution model for both conventional image sensors and single pixel cameras is described. A novel method for measuring resolution is then described and tested on simulated data and experimentaly.

The last section of the chapter concerns deconvolution. It presents the theory of deconvolution an the most popular algorithms and makes a comparison between them. Deconvolution via Compressive Sensing is considered. Also, a test of image deconvolution is described that demonstrates the effectiveness of deconvolution with kernel that was estimated with our method.

The forth chapter concerns the contributions to Hadamard spectroscopy. A summary of the principle of operation of Hadamard spectrometry is given then an implementation of a laboratory Hadamard spectroscope is described. An experimental evaluation method for the noise and Fellget advantage is presented together with experimental results. This part contains contributions from [6].

The third section of the chapter concerns microscanning, the use of multiple displaced images to create a new one with higher resolution. The technique and its advantages are presented and the Fellget advantage is derived. Numerical experiments on a database of spectra is then used to validate the usefulness of the technique and a laboratory experiment demonstrates its practicality. This section contains contributions from [8].

The last section of this chapter concerns the use of deconvolution on spectra. It compares the deconvolution algoritms already presented on a case where spectra where acquired using a microscanning technique. It contains contributions from [4].

The thesis ends with conclusions.

Chapter 2

Single Pixel Imaging

In the following the architecture of the Single Pixel Camera (SPC) is presented. The architecture for spectroscopy is very similar, only initial optical system is different.

The SPC is composed of three main parts: the imaging optical system (like the one on traditional cameras), the Spatial Light Modulator (SLM) and the radiation sensor giving the measurements. It also needs a computer in order to reconstruct a usable image.

In Figure 2.1 a typical SPC is shown, the first part of the setup, from the laser up to the object is not considered part of the camera. The first mirror is the optical system that projects an image of the object on the SLM which in this case is a Digital Micromiror Device (DMD). The SLM redirects light from certain areas of the image through a focusing mirror to a detector for measurement while light from all other areas is prevented from reaching the sensor. The focusing mirror simply insures that all the light redirected from the SLM falls on the active area of the detector.

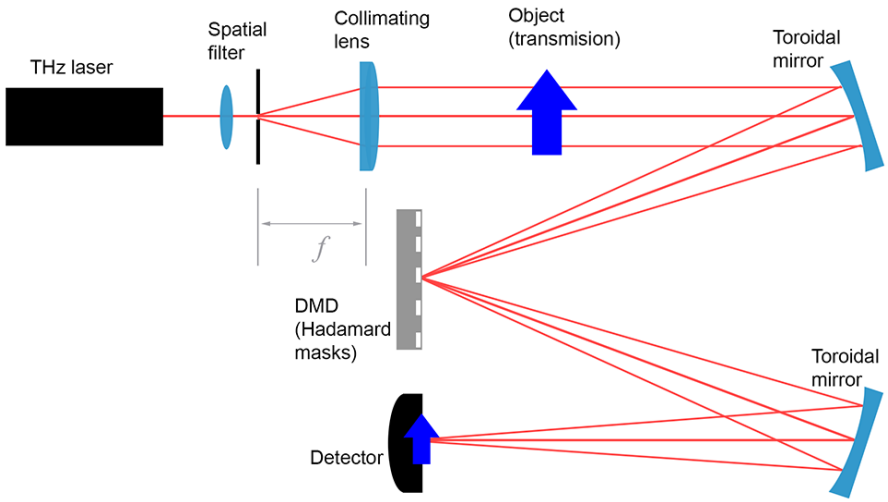

Figure 2.1: Basic diagram of a SPC in the Terahertz domain. Courtesy of Florin Garoi.

The SLM is reconfigured before each measurement according a predefined set of test functions. In this way, the camera acquires a series of measurements y_i that are scalar products between the image of the scene and the test functions. Expressed mathematically,the measurements are:

$$\mathrm{y}_i = \iint_{-\infty}^{+\infty} f(u,v)\phi_i(u,v)dudv, i = 1, \ldots, M \tag{2.1}$$

where (u, v) are spatial coordinates, f is the image of the scene projected onto the SLM, ϕ_i are the test functions, y_i are the measurements and M is the number of measurements taken by the system. Each measurement is taken with another test function.

The test functions are constrained by the construction of the SLM. These devices are composed of cells with identical shape that can transmit or block the light.

The sampled form of the image f is $\mathbf{x} = [\ \mathrm{x}_1, ..., \mathrm{x}_N\ ]^T$ where:

$$\mathrm{x}_j = \iint_{-\infty}^{+\infty} f(u,v)(\delta_j * c)(u,v)dudv \tag{2.3}$$

By substituting $\phi_i(u, v)$ from Equation (**??**) and taking into account Equation (2.3), Equation (2.1) becomes:

$$\mathrm{y}_i = \sum_{j=1}^{N} \Phi_{i,j}\mathrm{x}_j \tag{2.4}$$

The image of the scene is reconstructed from the measurements $\mathbf{y} = [y_1, ..., y_M]^T$. All reconstruction methods aim to solve Equation (2.4), where the measurement matrix has various forms. The methods we have used are Basis Scan (BS) and Compressive Sensing (CS) [10].

2.1 Basis Scan

In BS, the test functions are designed such that the measurement matrix has an inverse. The reconstruction is done by simply applying the inverse transformation to the measurements. The advantage of this method is that the measurement matrix can be designed to increase the image SNR considerably when compared to a standard camera. The measurement matrix is determined by the construction of the SLM. If it allows for negative coefficients to be implemented. The Hadamard matrix is used if the coefficients need to be positive then an S-matrix is used.

2.2 Compressive sensing

Compressive sensing (CS) is a new theory that provides a framework for the reconstruction of signals from fewer measurements than predicted by the Nyquist-Shannon sampling theorem.

The Nyquist-Shannon Theorem has provided a way to reconstruct continuous band limited signals from periodic samples. If a low band signal with a maximum frequency B is acquired by taking periodic samples with 2B one can reconstruct the original signal. The method of reconstruction is a simple linear filtering that can be performed with analog devices.

In contrast, CS concerns the reconstruction of discrete signals from global measurements, each measurement encompases the entire scene. There are two main premises on which CS relies [3]:

1. The original signal is sparse.

2. The test fuctions are incoherent with the signal.

What is meant by sparse is that there is a frame Ψ such that the signal can be represiented as:

$$\mathbf{x} = \Psi^T \mathbf{s} \tag{2.17}$$

where $\mathbf{s}$ is a vector with few non-null entries. If this has K or fewer non-null elements it is called K-sparse.

Incoherence means that if the signal is sparse in the first domain it is not sparse in the other domain (i.e. the domain of the measurements) and that the opposite is also true. The classic example of incoherence is that between the time domain and the frequency domain.

Thus the problem can be stated mathematically as the following:

$$\mathbf{y} = \Phi\mathbf{x} = \Phi\Psi^T\mathbf{s} \text{ while } \|\mathbf{s}\|_0 \leq K \tag{2.19}$$

where $\|s\|_0$ is the number of non-null elements in s. The signal of interest is x but the best way to solve the problem is to find s and then apply the Ψ transform. If we knew which elements are non-null the problem could be solved in a trivial manner so the challenge is in fact finding the non-null elements [10]. Eficient algorithms have been developed that can solve the problem by relying on the incoherence property. Among these there are Compressive Sampling Orthogonal Matching Pursuit (CoSaOMP) [18] and Iterative Hard Thresholding (IHT) [2].

Sparsifying transforms have been developed in the domain of signal compression. The most famous of these is the DCT transform used for storing images in the JPEG format or sounds in the MP3 format. More effective transforms have been developed more recently such as wavelet transforms or overcomplete dictionaries.

The signals do not actually need to be strictly sparse but compressible meaning that most of the energy of the signal has to come from a few coefficients. The rest of the coefficients can be neglected and considered noise [10].

Chapter 3

Imaging optics and resolution

This chapter presents my contributions to single pixel camera resolution evaluation and improvement. The first section introduces the principle of operation and the resolution model common to both conventional image sensors and single pixel cameras. It also presents different methods of measuring the resolution characteristics.

The second section presents my resolution model for the single-pixel camera. It details the influence of the SLM on resolution. The findings of this section were published in [7].

In the third section, my method for estimating the PSF is presented. The method is taylored for use on a single-pixel camera and its original elements are the use of an ellipse model in order to provide robustness to geometrical distortions and the use of the inverse Radon tranform to estimate the PSF. There is also a validation of the method by numerical simulations and a physical experiment. This method was published in [5] and [7].

The last section of the chapter concerns deconvolution. It presents the theory of deconvolution and the most popular algorithms making a comparison between them. Deconvolution via Compressive Sensing is compared with deconvolution applied on the reconstructed image. Also, a test of image deconvolution is described that demonstrates the effectiveness of deconvolution with a kernel that was estimated with our method. The results of this section are also published in [7].

3.1 The model of Single Pixel Camera PSF

In this section I derive the mathematical model of single pixel camera PSF. The model takes into account the optical system, aberrations caused by defocus (slight misalignment of SLM) and the shape of the SLM cell.

The image pojected on the SLM, f in equation (2.3), is itself an imperfect version of the ideal projection of the scene. It is the result of the convolution between the ideal projection of the scene f_0 and the PSF h_0 of the optical system:

$$f(u,v) = (f_0 * h_0)(u,v) \tag{3.8}$$

If in (2.3), we commute the convolution factors and substitute f, the image degradation process appears as a repeated convolution of f_0 with h_0 and c:

$$\mathrm{x}_j = \iint_{-\infty}^{+\infty} (f_0 * h_0 * c)\delta_j(u, v)dudv \tag{3.9}$$

Hence the end-to-end PSF is:

$$h = h_0 * c \tag{3.10}$$

In modelling the optical system, we start by considering that it is diffraction limited and integrating the effects of aberrations, we then model the SLM contribution in equation (3.10) as a PSF c with the shape of SLM cells. For our setup, which emploies a DMD, c will be rectangular. Consequently, the end-to-end PSF of the optical system will be the convolution between a circular and a rectangular PSF. Depending on SLM contribution, the end-to-end PSF can degenerate from a circular shape to a rectangular one. In our experiment, the end-to-end PSF resulted practically circular.

3.2 Our method for the measurement the camera PSF

Our estimation of the PSF is based, as in [1], on the image of a chart taken by the camera to be characterized. The chart consists in a white disk on a dark background. The illumination of the chart should be as uniform as possible otherwise a shading correction has to be done. The only distortion that we consider is an affine transform that turns the circular disk into an ellipsoidal one. Such distortions are caused by slight misalignments that could appear accidentally during the experiment.

A few auxiliary functions are used in the process of measuring the PSF. The first is the Line Spread Function (LSF), which is the response of the instrument to a narrow bright line. It is frequently used to project the PSF on one dimension. The LSF changes with the orientation of the line, it can be computed by integrating the PSF along the axis that is perpendicular to the line. We infer that the LSF as a function of the line orientation is the Radon transform of the PSF. Thus the PSF can be obtained from a large enough set of LSFs by the inverse Radon transform.

We will also use the Edge Spread Function (ESF) which is the result of acquiring an ideal step edge that goes from 0 to 1. The LSF can be obtained from the ESF by differentiation.

Having the image of the chart, the steps of the PSF measuring are the following:

1. The edge pixels are detected.

2. Then the shape of the edge is estimated by fitting an ellipse to the edge pixels.

3. Next, the ESF is estimated from the pixels in the vicinity of the edge. To this end, a point cloud is made, each point is made from a pixel by taking three parameters:

   (a) Intensity.

   (b) Displacement to the ellipse (negative for interior pixels, positive for the rest).

   (c) Orientation of the segment that connects the pixel with the ellipse.

4. In order to obtain the ESF for a finite set of distances and orientations, the cloud of points is uniformly resampled.

5. The LSF with respect to edge orientation is estimated by differentiating across the displacement dimension.

6. The PSF is then obtained by applying the inverse Radon transform of the LSF set.

The uniform sampling at step 4 is done by using kernel regression with a Gaussian kernel with σ being 0.4 of the sampling period.

By setting the sampling rate of the ESF we obtain the same sampling rate for the estimated PSF. The sampling rate can be higher than that of the test image as long as there are enough pixels to perform kernel regression. The sampling rate for the orientation is such that the number samples of the ESF is the same as the number of samples of the PSF.

The following three new aspects have been introduced compared to the algorithm in [1]. We use an ellipse to model for the original sharp image instead of a circle. This allows to take into account all affine distortions. We extract the angle of each pixel in addition to intensity and displacement. This supplementary information is the key for obtaining the LSF at various edge orientations. Finally, we perform the inverse Radon transform in order to estimate the PSF as opposed to estimating only the LSF.

3.2.1 Numerical simulations

I tested the PSF estimation method using numerical simulations. I used PSFs with four different shapes: disk, square, hexagon and rounded square.

The image of the circular chart was generated and tilt distortion was simulated with a tilt angle between 0° and 15°. The image was then blurred with a known kernel (one of the four PSFs), subsampled and corrupted with additive white Gaussian noise. The result has been a test image of 512×512 pixels simulating the acquisition by SPC. The PSF is estimated with the same sampling rate as the known kernel using the method in Section 3.2.

Figure 3.13 depicts the kernels used for simulation alongside the respective estimate. In this case, the kernels and the estimates have a sampling rate that is three times grater than the test image. It is evident that the estimates are smoother

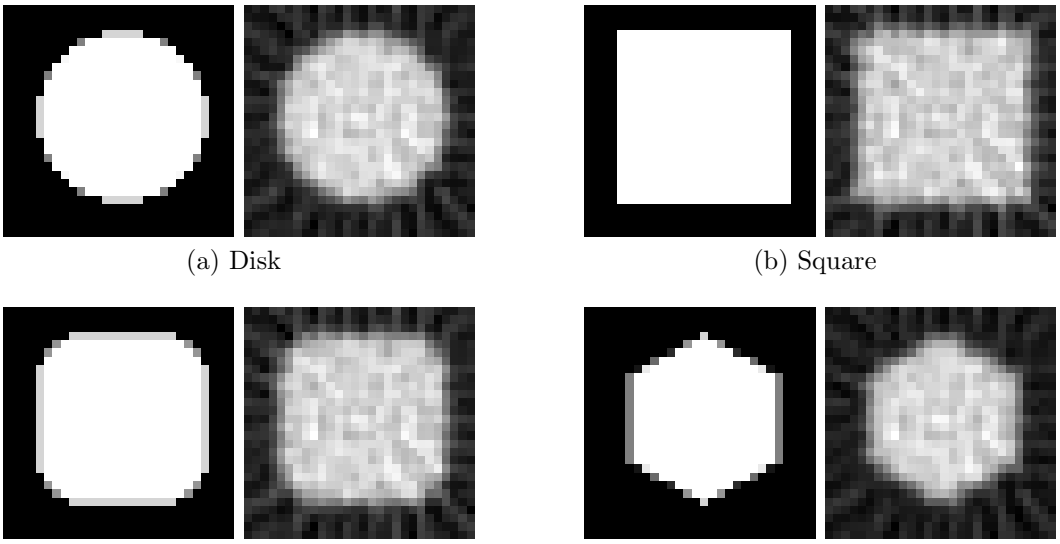

(a) Disk (b) Square

(c) Rounded Square (d) Hexagon

Figure 3.13: PSF estimation on synthetic images for different PSF shapes. Left: Original kernels used to generate the test images. Right: Kernels estimated with our method.

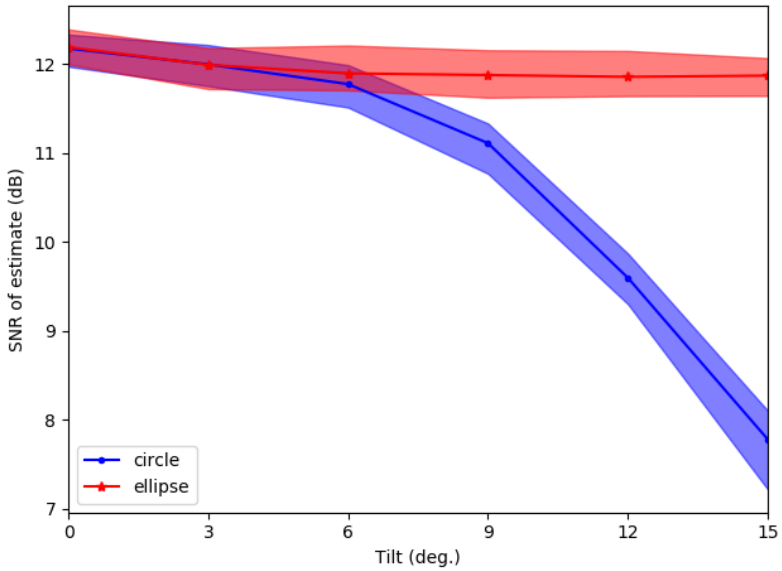

Figure 3.14: Comparison between estimation with a circle model of the edge and an ellipse model of the edge.

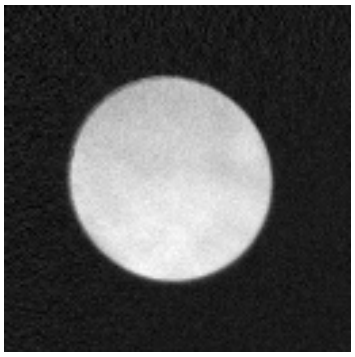

(a) Image reconstructed using BS.

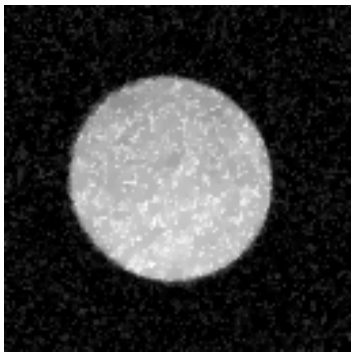

(b) Image reconstructed using CS with 50% of measurements

Figure 3.17: Different reconstructions of the chart acquired with our SPC setup.

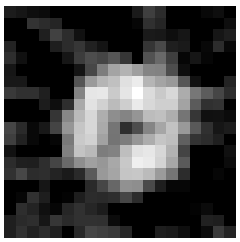

Figure 3.18: Experimental estimate of the PSF of our prototype.

than the original kernels and streaking artifacts are present but the estimate is good enough to discern the shape of the kernel.

In the next simulations only the hexagonal kernel was used. The accuracy of the estimation is given as a SNR calculated using the original kernel as the reference. For each setting 100 experiments were made and the 90% confidence intervals and the medians are plotted.

The effectiveness of tilt correction is shown in Figure 3.14. The SNR of the estimate is plotted versus the tilt in two cases: when fitting an ellipse on the edge and when fiting a circle. The ellipse model gives a significantly better result for tilts greater than 6°.

3.2.2 Experimental results

To experimentally measure the PSF, we used a laboratory model of a single pixel camera with a DMD as SLM. Light from a halogen lamp with a peak wavelength of about 1µm is "softened" with a photographic light diffuser and sent towards the object. The transmitted light goes towards the DMD. The image of the object is projected on the DMD with and objective lens of 30 mm diameter. The DMD is positioned at a distance of 82 mm from the lens. The light modulated by DMD is focused on the detector using a zoom imaging lens.

We acquired an image of an opaque screen with a 6 mm hole. The resulting image is shown in Figure 3.17 first using the BS reconstruction method then using CS with

50% of the total number of measurements. The image recontructed with BS is used for PSF estimation.

We measured the PSF of the setup using our method using the acquired image. The estimation was done with an oversampling ratio of 2. We compared it with the theoretical calculations in Section 3.1. Considering the effects of diffraction with $\lambda = 1\mu m$, $z = 82mm$ and $w = 30mm$, we found that the radius of the central lobe of the Airy disk is 0.4 µm. Since the DMD cells are 55 µm squares, the diffraction effects are negligible leaving only the cell shape and optical aberrations as important factors in determining the PSF.

The experimental PSF is depicted in Figure 3.18. The estimation was done with an oversampling ratio of 2. The shape suggests a spherical aberration of the objective lens.

3.3 Deconvolution via CS

Having a model for the degradation of the image we can improve it using inversion methods. While conventional deconvolution methods can not account for the particular camera architecture, the CS framework can work with any linear model so it can be adapted to multiple tasks. Consequently, a strategy for deconvolution is to include the PSF of the camera in the acquisition model:

$$\mathbf{y} = \Phi\mathbf{x} + \mathbf{n} = \Phi H\mathbf{x_0} + \mathbf{n} = \Phi^\star\mathbf{x_0} + \mathbf{n} \tag{3.25}$$

where $\mathbf{x}_0$ is the restored image and H is the blurring matrix that represents the convolution with the camera PSF.

With this model, the CS algorithm estimates the ideal image $\mathbf{x_0}$ instead of its blurred version $\mathbf{x}$. This strategy was used for the first time in [16] in the context of a curvelet regularization and Poisson Singular Integral deblurring operator.

If CS with TV is used and the scene is acquired with an array camera then the deconvolution via CS reduces to TV deconvolution. In this case the maximum entropy method is superior so a comparison between the maximum entropy deconvolution and deconvolution via CS is waranted.

I conducted a numerical experiment by simulating a SPC acquisition of the Chelsea test image from. A 128×128 crop of the image is blurred with a disk kernel and a CS acquisition with 4096 measurements is performed. The measurement matrix is composed of random lines from a Hadamard matrix. I then applied maximum entropy deconvolution to the CS reconstruction of the image and compared it with a CS reconstruction with deconvolution. The results of the reconstruction is shown in Figure 3.25. The decovolution via CS has higher SNR than both CS reconstruction with no deconvolution and CS reconstrution with deconvolution with the maximum entropy method.

It seems that deconvolution applied on a reconstructed is less effective because CS reconstruction introduces artifacts which affect the deconvolution method.

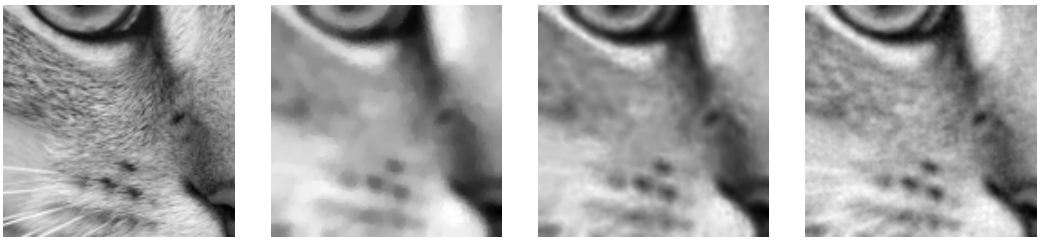

(a) Original

(b) CS reconstruction. SNR=19.0dB

(c) CS reconstruction and maximum entropy deconvolution. SNR=19.9dB

(d) Deconvolution via CS. SNR=21.7dB

Figure 3.25: Reconstruction of a test image blurred with the disk kernel.

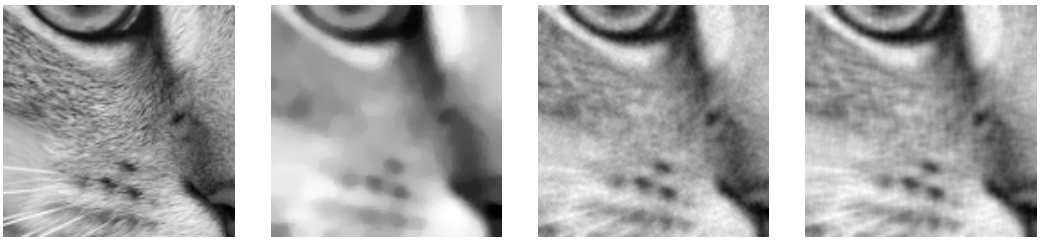

(a) Original

(b) No deconvolution.. SNR=18.89dB

(c) Deconvolution with true kernel. SNR=21.64dB

(d) Deconvolution with estimated PSF. SNR=21.62dB

Figure 3.26: Reconstruction of a test image blurred with the rounded square kernel.

3.3.1 Experiments with estimated PSF

In order to show the benefit of reconstructing the image using an estimated PSF, I conducted and experiment using the same crop of the Chelsea test image (Figure 3.26a). The image was blurred with the rounded square kernel illustrated in Figure 3.13. A CS acquisition was simulated by computing the scalar products of the image with 4096 random binary masks (1/4 of the number of pixels). Then three reconstructions were made using total variation regularization. The results along with the SNR of each reconstruction is shown in Figure 3.26. The first reconstruction (Figure 3.26b) reforms no deconvolution. The second one (Figure 3.26c) has the true kernel incorporated in the model. The third one (Figure 3.26d) has the estimated kernel incorporated. A visible improvement is shown in the images reconstructed with deconvolution. The image reconstructed using the estimated PSF is of practically the same quality as than the one reconstructed using the true kernel ,the difference being 0.02dB.

Chapter 4

Hadamard Spectrometry

The aim of spectrometry is to measure the intensity of light as a function of wavelength. A traditional spectrometer has five main components: entrance aperture, the collimating optics, a dispersive element (usually a grating), the focusing (or imaging) optics and a detector. The light from the source is directed by the entrance aperture into the collimating optics. The latter ensures that the light rays are parallel while hitting the dispersing element. The dispersed light will leave the dispersive element at different angles depending on the wavelength. Then the focusing optics creates an image of the spectrumat the plane of the detector. The detector is usually a sensor array that captures the image but it can be a movable slit (an exit aperture) followed by a single detector that measures a single wavelength at a time [15, p 20 - 24].

In the design stage, a few tradeoffs have to be considered. One of the tradeoffs is in choosing the size of the detector. If the detector is large or the slit is more open then the signal is high in comparison with the sensor noise but a large sensor blurrs the spectrum since the detector receives a wider range of wavelengths. Another design tradeoff is in the size of the entrance aperture. The image of the spectrum is created by the image of the aperture convolved with the latent spectrum of the light. If the aperture is small the spectrum is well represented but little light is left in so the signal to noise ratio will be lower.

An alternative method that partially eliminates this tradeoff is Hadamard spectrometry. It can be implemented either by using mechanical masks or

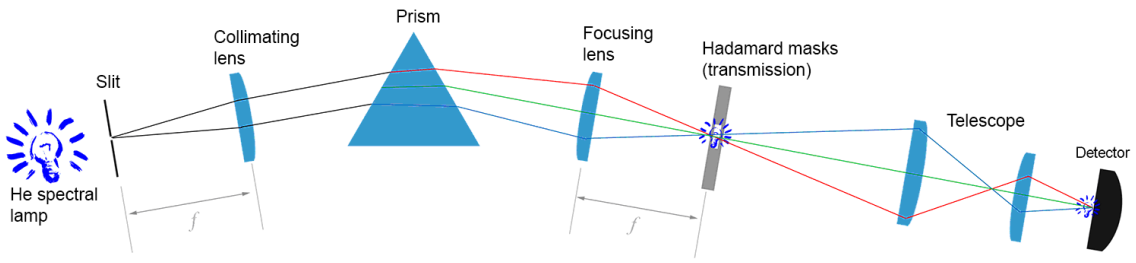

Figure 4.3: The basic diagram of a Hadamard spectrometer.

micro-mechanical mirrors or shutters. An example with mechanical masks is shown in Figure 4.3. The mask is placed in the place of the exit slit. A controllable mixture of wavelengths reaches the detector to be measured and a set of measuremens is taken with diferent masks. The resulting set of measurements is linked to the original spectrum by a linear transform with coefficients of 0 or 1 [15, p. 29 - 32]. The coefficients correspond, for example, to the shut or open states of micro-shutters or to two positions of micro-mirrors. Using a computer one can find the spectrum by applying the appropiate inverse transform.

The main advantage of this method is that more light hits the detector since a mixture of wavelengths are measured [15, p. 27]. If the noise is aditive then the final SNR of the spectrum will be much lower than that of a spectrum acquired by despersive spectroscopy. This effect is called the Fellget advantage or the multiplex advantage.

Until recently, this method needed a cumbersome set of mechanical masks but with the advent of the DMD practical applications will be feasible. Hadamard spectrometry had gathered attention especially in imaging spectroscopy where Hadamard multiplexing is applied in the spatial domain [14]. The IRIMOS instrument, an imaging spectroscope designed for astronomy, has successfully used a Hadamard mode of operation [13].

4.1 Experimental noise evaluation

I conducted experiments on an spectrometer prototype built by the Laser Interferometry and Applications (ILA) team at the National Institute for Laser, Plasma and Radiation Physics (INFLPR). The setup is presented in Figure 4.6. It represents a version of the Edbert-Fastie spectrometer modified for Hadamard spectrometry [12, 23, 6].

In order to evaluate the noise and Fellget advantage of our experimental model, the spectrum of on orange LED was measured 8 times by Hadamard spectroscopy and 8 times by dispersive spectroscopy. Dispersive spectroscopy is implemented by activating a single DMD cell for each measurement. Each measurement consists in 127 samples. The measurements made by dispersive spectroscopy are in the range of 0.06 to 0.13 V and masurements made by Hadamard spectroscopy in the range of 0.2 to 0.4 V. Figure 4.8 shows two identical spectra measured through dispersive spectroscopy and two such spectra reconstructed through Hadamard spectroscopy. One can see first that the background intensity is much lower with Hadamard spectroscopy. The cause is that the dark current is smaller compared with the level of the measured Hadamard coefficients than with the measurements of dispersive spectroscopy. It is to note the significantly higher noise in the case of dispersive spectroscopy.

We estimated the noise in three cases: measurements by dispersive spectroscopy, measured Hadamard coefficients and the numerically reconstructed spectra. Sixteen measurement sets where taken for the first two cases. The third case was made from the measurements of the second case. Since each set of measurements had a different offset the mean of each set was extracted then the signals where grouped in pairs and 8

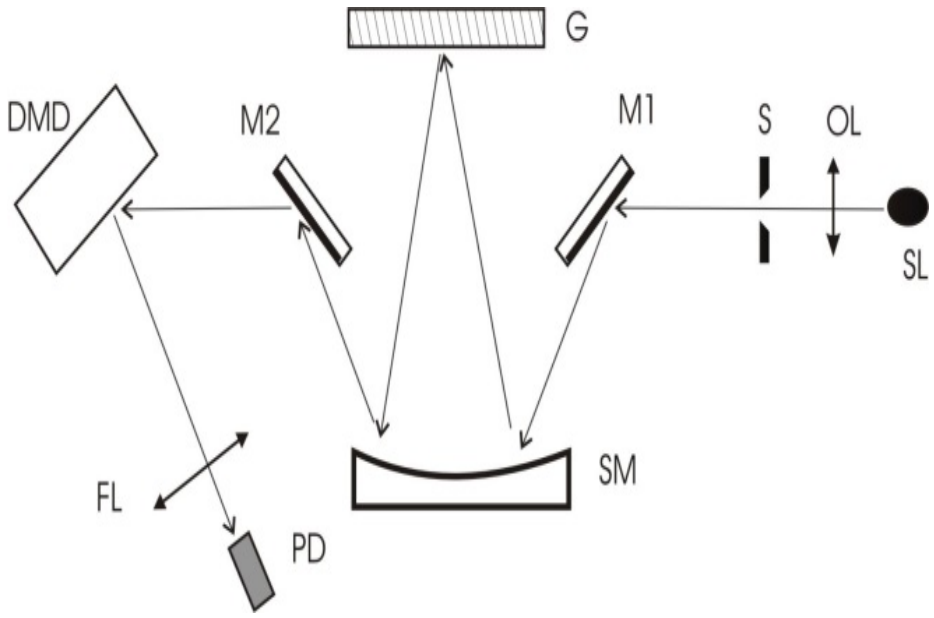

Figure 4.6: Experimental set-up. SL – LED, OL - objective lens, S - entrance slit, M1,2 –deflection mirrors, SM- spherical mirror, G- blazed grating, DMD- Digital Micromirror Device, FL- focusing lens, PD – photodetector. Courtesy of Tiberius Vasile.

Table 4.1: Estimated noise standard deviations.

Measurements	Standard deviation (mV)
Dispersive spectroscopy	3.00
Hadamard coefficients	4.80
Hadamard spectroscopy	0.85

independent noise sets where made for each case. The estimated standard deviations of the noise are given in Table 4.1. The relative error calculated for $L = 4 \times 127$ is 5%. The noise in Hadamard spectroscopy is considerably lower (0.85 mV) than in the case of dispersive spectroscopy (3.00 mV) although the measured Hadamard coefficients have a higher noise (4.80 mV).

The gain in accuracy calculated is 3.52 and the relative error of the estimate is 0.1 The gain is well bellow the theoretical Fellgett advantage, which is 5.68 in the case of $N = 127$.

The explanation for the poorer gain is that the detector has varying noise levels. At low intensity measurements (case of dispersive spectrometry) the noise standard deviation is 3 mV while at high intensity measurements (case of Hadamard coefficients) it is 4.80 mV. This indicates that the noise level varies as a function of the of the signal intensity. The noise level increases by a factor of 1.6 for an increase of an order of magnitude in the intesity of the signal.

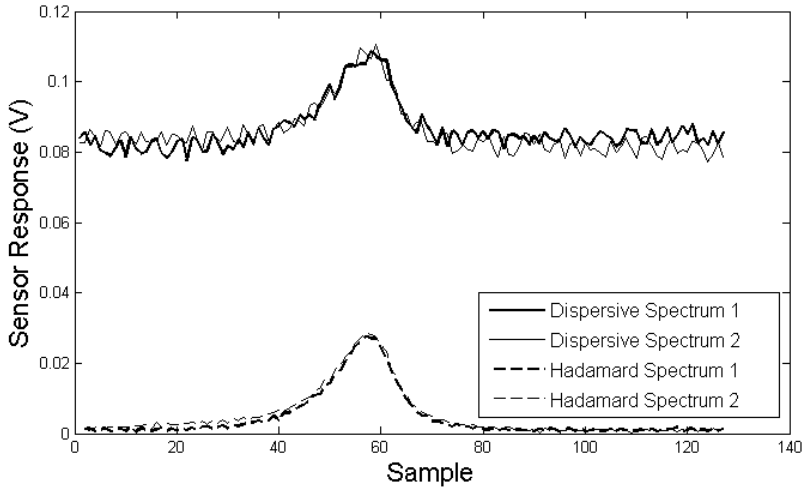

Figure 4.8: Pairs of measurements obtained by dispersive spectroscopy and Hadamard spectroscopy

4.2 Microscanning in Hadamard Spectrometry

The noise reduction effect of Hadamard spectroscopy has enabled the acquisition of spectra in difficult wavelength domains such as far-infrared. A drawback is that the SNR still decreases with resolution, even if it decreases at a slower pace than with classical spectroscopy. One might want to obtain a lower noise level even if the acquired spectra loses a bit of detail through blurring. The normal technique used would be to filter the spectrum after acquisition but in this chapter we demonstrate that by using a technique called microscanning one can obtain a better result than filtering at the cost of changing the mask set.

In order to implement the microscanning technique no additional components are needed except for a modified set of masks. If we want to get a microscan spectrum of N samples from K previews then K sets of Hadamard masks with N/K samples should be made. Each set is a shifted version of the previous one with the shift being 1/K of the pixel pitch. To generate the high resolution spectrum the low resolution spectra are interpolated to the desired resolution then co-registered and averaged.

An illustration of microscanning for two previews is presented in Figure 4.10. In this illustration, the Hadamard transforms are ignored for simplicity. The first step consists of acquiring the previews. Each sample of the a preview covers an area equivalent to two samples at the final resolution so the intensity of that area is "summed" during the acquisition. The first preview measures the intensities at certain positions and the second preview measures the intensities at positions that are shifted by one sample at final resolution. The next step is interpolation. In this step the resolution of the two previews is enlarged by doubling each sample. In the coregistration, summation and scaling steps, the information from both of the previews is combined and the resulting signal is richer in information than the previews.

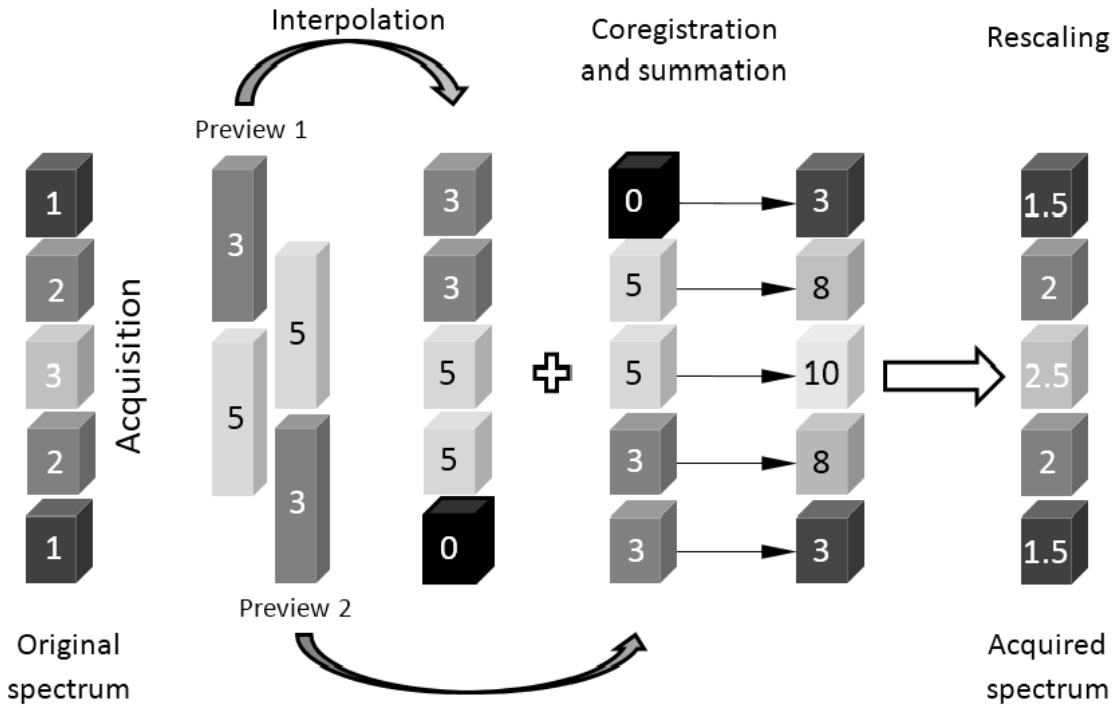

Figure 4.10: Illustration of the microscanning process.

The microscanning process introduces a blurring effect that reduces the contrast of the fine details of the spectrum. In noiseless conditions, microscanning is mathematically equivalent to acquiring the spectrum at high resolution then filtering it with the following kernel[21]:

$$h(d) = \begin{cases} \frac{K-|d|}{K^2}, & |d| < K \\ 0 & otherwise \end{cases} \tag{4.14}$$

where d is the distance from the current sample and the weighted sample.

In the following I will analyze the noise reduction effect of the microscanning method. The reconstruction of the high resolution spectrum from microscanning measurements can be expressed as:

$$\hat{x}_j^{(MS)} = \frac{1}{K^2} \sum_{k=1}^{K} \sum_{i=1}^{N/K} b_{j,i} \left(y_{i,k} + n_{i,k} \right) \tag{4.15}$$

where $y_{i,k}$ is the i-th measurement of the k-th preview, $b_{j,i}$ is the i-th reconstruction weight corresponding to the j-th high resolution sample and $n_{i,k}$ are the corresponding noise components. The values of the reconstruction weights are $b_{j,i} = \pm K/N$. The value of the reconstructed samples is divided by K^2 because two summations are carried out that raise the peak signal: one is explicit in the equation above and one is implicit because the size of the pixels used in the microscanning method is K times larger.

If we separate the noise from the useful signal, we get:

$$\hat{x}_j^{(MS)} = x_j^{(MS)} + \frac{1}{K^2}\sum_{k=1}^{K}\sum_{i=1}^{N/K} b_{j,i}n_{i,k} \tag{4.16}$$

One can deduce that the standard deviation of the noise after reconstruction is:

$$\sigma_{MS} = \frac{\sigma}{K^2}\sqrt{\sum_{k=1}^{K}\sum_{i=1}^{N/K} b_{j,i}^2} = \frac{\sigma}{K^2}\sqrt{N\frac{K^2}{N^2}} = \frac{\sigma}{K\sqrt{N}} \tag{4.17}$$

By comparing the result of the previous equation with the result in Equation 4.17, we find that a noise reduction by a K factor has been achieved. The noise reduction is not generated only by the filtering effect of the method. To prove this we consider a spectrum acquired at high resolution with the basic Hadamard method that has been filtered with the equivalent kernel from equation 4.14. The samples of the spectrum noise are i.i.d. random variables with standard deviation σ_H as in equation 4.17. From the definition of filtering with a discrete kernel we get the following standard deviation for the noise of the spectrum:

$$\sigma_F = \sigma_H\sqrt{\sum_{d=1-K}^{K-1}\left(\frac{K-|d|}{K^2}\right)^2} = \sigma\sqrt{\frac{2K^2-1}{3K^3N}} \approx \frac{\sigma}{\sqrt{1.5KN}} \tag{4.18}$$

This result proves the advantage of using microscanning techniques to reduce noise. One can conclude that by simply increasing the number of previews K one can infinitely improve the SNR while maintaining the same resolution. While technically correct one has to keep in mind that while the number of samples per area is the same, the level of detail of the spectrum decreases.

4.2.1 Numerical experiments

In order to evaluate the effectiveness of the microscanning method, I performed simulated acquisitions based on 98 different mineral spectra taken from the Mineral Spectroscopy Server [19]. For each spectrum, acquisitions with different sensor noise levels were simulated using both the classic Hadamard method and the Hadamard method with microscanning with 2 or 4 previews. The accuracy of the acquisitions was then evaluated using the SNR.

The behavior of the results for all the tested spectra is similar to the one illustrated in Figure 4.12. One can see that the SNR of the Hadamard acquisitions decreases linearly with noise level, while in case of the Hadamard with microscanning approach, the behavior, although decreasing, is not linear. If the noise is low, the classic Hadamard acquisition performs better because the microscanning acquisitions reduce the contrast of finer details. Beyond a certain threshold, the noise reduction of the microscanning method outweighs the contrast reduction and the microscanning acquisition becomes better than the classic Hadamard acquisition. At higher noise

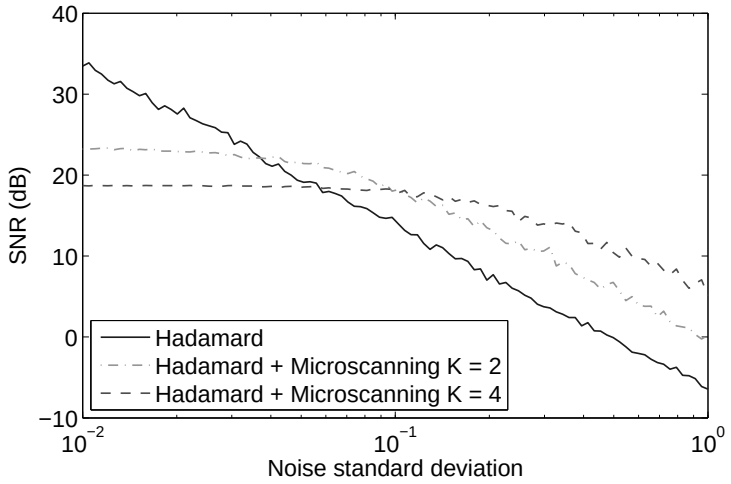

Figure 4.12: SNR of simulated acquisitions of high resolution Hadamard and low resolution Hadamard with microscanning for the far infrared spectra of Chalcocite.

levels (in our example for $K = 2$ and a noise deviation over 10^{-1}) the SNR of the microscanning acquisition starts to decrease steadily. At that point a microscanning acquisition with more previews would further increase the SNR (in our example if we use $K = 4$). A critical value of this behavior is the SNR of the Hadamard method obtained at the threshold where the microscanning method becomes more accurate. This value changes for every spectra and choice of K.

The critical SNR for $K = 2$ for almost all the spectra on which we experimented is over 20 dB, exceptions being the spectra for water and pyrite. The median value of the critical SNR is 32 dB. Consequently a large portion of the spectra could benefit from the microscanning method at average noise levels.

4.2.2 Physical experiment

The spectrum was measured using a set of high resolution Hadamard masks providing a 1024 sample spectra. Two sets of low resolution Hadamard masks providing 512 sample previews were used to capture a high resolution spectra with the microscanning method. The masks for second low resolution spectrum are identical to the first except for displacement of one DMD micromirror to the right.

We calculated the Contrast to Noise Ratio (CNR) of the spectra using the following equation:

$$\mathrm{CNR} = 10 * \log_{10}\left(\frac{N(S_A - S_B)^2}{\sum_i (x_i - \hat{x}_i)^2}\right) \tag{4.22}$$

where N is the number of samples, S_A is the average intensity of the signal and S_B is the average intensity of the background.

For the signal intensity we considered the area of the two spectral lines. The noise standard deviation was estimated on a large flat area not shown in the figure. It is $5.95 \times 10^{-5}V$ for classic Hadamard, $3.44 \times 10^{-5}V$ for microscanning and $4.14 \times$

Method	D_{KL}	SNR_{dB}	**Method**	D_{KL}	SNR_{dB}
No deconvolution	0.177	5.83	L1 minimization	0.070	13.5
Wiener filter	0.073	11.6	Lucy-Richardson	0.098	15.5
Total Variation	0.094	13.2	Maximum Entropy	0.061	18.5

Table 4.2: Kullback-Leibler Divergence and Signal-to-Noise Ratio measured for the tested deconvolution algorithms.

$10^{-5}V$ for filtered Hadamard. The CNR is 20.4dB for classic Hadamard, 25.1dB for microscanning and 23.5dB for the filtered spectrum. Microscanning improves the CNR by 4.7dB comparing with classic Hadamard and by 1.6dB comparing with filtered Hadamard.

4.3 Deconvolution of spectra

Microscanning can be combined with deconvolution in order to obtain a better estimation than the tradeoff between blurring and noise reduction generated by simple microscanning. The effectiveness of such a procedure depends on the spectrum and the deconvolution algorithm. In this section four algorithms are tested in such a scenario to determine whether the combination provides significant advantages.

In order to have a reference for our results, we use a visible domain spectrum that is blurred and undersampled according to a spectrometer model. We simulate microscanning and we restore the high resolution spectrum by applying the deconvolution algorithms.

The reference spectrum was obtained by extracting a line from the spectrographic image of a helium spectral lamp. We selected for testing the central part with two spectral lines and we supposed that it represents a THz band, already oversampled by acquisition of 8 shifted measurements. The signal was smoothed with a kernel (LSF) calculated assuming diffraction limited optical components with a f-number of 2 and a wavelength of 8 samples. AWGN noise was added with a Signal-to-Noise Ratio (SNR) of 30 dB.

The results obtained with the deconvolution listed in Table 4.2. The accuracy of the restored signal is measured by Kullback-Leibler divergence D_{KL} and SNR.

All deconvolution algorithms give significant errors especially for the highest peak but some work better than others. The Wiener filter has high ringing effects compared to the other methods. Total Variation provides an estimate that is piecewise constant so is does not represent the peaks properly. L1 minimization with wavelets gives an estimate with lots of spikes in regions where the spectrum is smooth. The Lucy-Richardson deconvolution gives a more accurate representation of the signal but some ringing is still visible. The best accuracy is achieved by MEM deconvolution, the shape of the peaks being closer to the real spectrum even if it still has some ringing.

Chapter 5

Conlusions

The thesis presents contributions to the field of computational imaging, on single pixel imaging and multiplexed spectrometry. The focus is on the evaluation and improvement of camera and spectrometer parameters.

The architectures in question where explained in detail and the comonalities between them where highlighted. Consequently, the techniques developed in one of the architectures can be transfered to the other. With respect to noise the two architectures are nearly identical while the aspects related to resoluton can easily be translated from the single pixel camera to the multiplexed spectrometer.

In the applications of spectrometry, having a low noise level is especially important. Multiplexed spectrometry is used for its capability of increasing the signal-to-noise ratio known as the Fellget advantage. I have studied the noise behaviour of a laboratory implementation experimentally and concluded that while the Fellget advantage plays a significant role other effects increase the noise level above the expected threshold.

I have extensively studied the noise reduction approach known as microscanning in the context of Hadamard spectrometry. I have derived a relationship between the previews taken and the noise reduction. I have then studied the tradeoff between the blurring induced by the method and the noise reduction effect using both simulations and laboratory experiments. I concluded that, for most spectra, the method is capable of producing more accurate spectra than a simple Hadamard method.

For the single pixel camera we developed a model for the PSF and MTF of the system taking into account different optical effects. Then, I proposed a method to measure the PSF experimentaly that takes into account the paricularities of single pixel cameras. The main chalanges that I adressed where that the images that the camera produced where of low resolution and that they would most likely be affected by tilt. Numerical simulations were done to test the accuracy of the method, then the method was used to get the PSF of a single pixel camera prototype.

Since the PSF can be obtained experimentally, an oportunity arises to use the new information to produce a better estimate of the scene. To this end, I investigated several deconvolution methods allong with the integration of the measured PSF into the CS reconstruction method. Integrating the PSF into the reconstruction proved to be the most effective method.

5.1 Original contributions

To summarize, my contributions to the development of the computational imaging sensors are:

- A mathematical model for the PSF of the single pixel camera. The model takes into account the shape of SLM cell as well as the imaging optics and the wavelength of the measured light [7].
- A method for measuring the PSF of single pixel cameras is developed that is resistent to projection distortions and noise. The method is evaluated using simulations and tested experimentaly [5], [7]..
- A number of deconvolution algorithms are considered and the fesability of deblurring images using the Point Spread Function (PSF) obtained from the resolution measurement are tested and confirmed.
- An experimental study is conducted on the noise suppresion capabilities of the Hadamard transform. The study finds that the noise supression capabilities are mitigated by sensor nonlinearities [6].
- Microscanning, a method for further suppresing noise while sacrificing some detail, is mathematically moddeled. A theoretical analysis of the noise supression effect is conducted. The benefits and drawbacks for spectrometry are studied using simulations and demonstrated experimentaly. The method proves to be useful in cases where the noise is significant such as far infrared spectrometry [8].
- A study of different deconvolution methods applied to spectrometric data is conducted. The Maximum Entropy Method (MEM) and Total Variation (TV) regularisation are found to be the best candidates [4].

5.2 Published papers

5.2.1 Journal papers

1. Cristian Damian, Florin Garoi, Cristian Udrea, and Daniela Coltuc. The evaluation of single pixel camera resolution. *IEEE Transactions on Circuits and Systems for Video Technology*, pages 1–1, 2020. Impact Factor 4.13, Q1, WOS:000557386300018

2. Cristian Damian, Adrian Sima, Tiberius Vasile, and Daniela Coltuc. Microscanning in hadamard spectroscopy. *Applied Optics*, 56(18):5211, jun 2017. Impact Factor 1.79, Q3, WOS:000403821500014

3. Florin Garoi, Cristian Udrea, Cristian Damian, Petronela Prepelita, and Daniela Coltuc. Thz laser beam profiling by homogeneous photodoping of high resistivity silicon in a compact single-pixel detection setup. *IEEE Transactions on Terahertz Science and Technology*, 9(2):200–208, mar 2019. Impact Factor 2.59, Q2, WOS:000460746900011

4. M. A. Petrovici, C. Damian, and D. Coltuc. Maximum entropy principle in image restoration. *Advances in Electrical and Computer Engineering*, 18(2):77–84, 2018. Impact Factor 1.1, Q4, WOS:000434245000010

5.2.2 Conference papers

1. Cristian Damian and Daniela Coltuc. Measurement of non-circular PSFs in single pixel cameras. In *2018 International Conference on Communications (COMM)*, pages 1–124. IEEE, jun 2018. WOS:000449526000021

2. C. C. Damian, D. Coltuc, F. Garoi, and M. Datcu. Improvement of submillimeter spectrometric measurement via deconvolution. In *2017 International Symposium on Signals, Circuits and Systems (ISSCS)*. IEEE, jul 2017. WOS:000380451600086

3. Cristian Damian, Alexandru Crisan, Tiberius Vasile, Daniela Coltuc, and Victor Damian. Noise evaluation in hadamard spectroscopy. In *2015 International Symposium on Signals, Circuits and Systems (ISSCS)*, pages 1–4. IEEE, jul 2015. WOS:000380451600086

4. Mihai-Alexandru Petrovici, Cristian Damian, and Daniela Coltuc. Image reconstruction from incomplete measurements: Maximum entropy versus l1 norm optimization. In *2017 International Symposium on Signals, Circuits and Systems (ISSCS)*. IEEE, jul 2017. WOS:000425211500024

5. Mihai-Alexandru Petrovici, Cristian Damian, Cristian Udrea, Florin Garoi, and Daniela Coltuc. Single pixel camera with compressive sensing by non-uniform sampling. In *2016 International Conference on Communications (COMM)*. IEEE, jun 2016. WOS:000383221900091

6. Florin Garoi, Cristian Udrea, Cristian Damian, Petre C. Logofătu, and Daniela Colţuc. Assessment of illumination conditions in a single-pixel imaging configuration. In Marian Vladescu, Razvan Tamas, and Ionica Cristea, editors, *Advanced Topics in Optoelectronics, Microelectronics, and Nanotechnologies VIII*. SPIE, dec 2016. WOS:000391359600037

5.2.3 Other papers

1. Andrei Valeanu, Cristian Damian, Cristina Daniela Marineci, and Simona Negres. The development of a scoring and ranking strategy for a patient-tailored adverse drug reaction prediction in polypharmacy. *Scientific Reports*, 10(1), jun 2020. Impact Factor 4, Q1, WOS:000543969200033

2. C. Damian and D. Coltuc. Generative adversarial networks for total electron content prediction. *2020 International Symposium on Electronics and Telecommunications (ISETC)*, pages 1–3, 2020. WOS:000612681000015

3. Cristina Popa, Daniela Coltuc, and Cristian Damian. On the watermarking of image compressed samples. In *2019 International Symposium on Signals, Circuits and Systems (ISSCS)*. IEEE, jul 2019. WOS:000503459500045

4. Cristian Damian and Daniela Coltue. Print signatures for documents using EU logo. In *International Symposium on Signals, Circuits and Systems ISSCS2013*. IEEE, jul 2013. WOS:000337926700071

Bibliography

[1] Richard L. Baer. Circular-edge spatial frequency response test. In Yoichi Miyake and D. Rene Rasmussen, editors, *Image Quality and System Performance*, volume 5294, pages 71–81. SPIE, dec 2003.

[2] Thomas Blumensath and Mike E. Davies. Iterative hard thresholding for compressed sensing. *Applied and Computational Harmonic Analysis*, 27(3):265–274, nov 2009.

[3] E. J. Candes and M. B. Wakin. An introduction to compressive sampling. *IEEE Signal Processing Magazine*, 25(2):21–30, March 2008.

[4] C. C. Damian, D. Coltuc, F. Garoi, and M. Datcu. Improvement of submillimeter spectrometric measurement via deconvolution. In *2017 International Symposium on Signals, Circuits and Systems (ISSCS)*. IEEE, jul 2017.

[5] Cristian Damian and Daniela Coltuc. Measurement of non-circular PSFs in single pixel cameras. In *2018 International Conference on Communications (COMM)*, pages 1–124. IEEE, jun 2018.

[6] Cristian Damian, Alexandru Crisan, Tiberius Vasile, Daniela Coltuc, and Victor Damian. Noise evaluation in hadamard spectroscopy. In *2015 International Symposium on Signals, Circuits and Systems (ISSCS)*, pages 1–4. IEEE, jul 2015.

[7] Cristian Damian, Florin Garoi, Cristian Udrea, and Daniela Coltuc. The evaluation of single pixel camera resolution. *IEEE Transactions on Circuits and Systems for Video Technology*, pages 1–1, 2020.

[8] Cristian Damian, Adrian Sima, Tiberius Vasile, and Daniela Coltuc. Microscanning in hadamard spectroscopy. *Applied Optics*, 56(18):5211, jun 2017.

[9] RA DeVerse, RM Hammaker, and WG Fateley. Realization of the hadamard multiplex advantage using a programmable optical mask in a dispersive flat-field near-infrared spectrometer. *Applied Spectroscopy*, 54(12):1751–1758, 2000.

[10] M.F. Duarte, M.A. Davenport, D. Takhar, J.N. Laska, Ting Sun, K.F. Kelly, and R.G. Baraniuk. Single-pixel imaging via compressive sampling. *Signal Processing Magazine, IEEE*, 25(2):83–91, 2008.

[11] M Endemann. Mipas instrument concept and performance. In *Proceedings of the European Symposium on Atmospheric Measurements from Space*, volume 1, pages 29–43, 1999.

[12] Thomas Eversberg and Klaus Vollmann. *Reflecting Spectrographs*, pages 281–319. Springer Berlin Heidelberg, Berlin, Heidelberg, 2015.

[13] DJ Fixsen, MA Greenhouse, JW MacKenty, and JC Mather. Spectroscopy using the hadamard transform. In *Sensors, Cameras, and Systems for Industrial/Scientific Applications X*, volume 7249, page 72490X. International Society for Optics and Photonics, 2009.

[14] Nahum Gat, Tait Pottebaum, Gordon Scriven, and Rebekah Brandt. Hadamard transform imaging spectrometry (htis) and compressive detection techniques. In *Meeting of the Military Sensing Symposia (MSS) Specialty Committee on Passive Sensors*.

[15] Neil J.A. Harwit, Martin; Sloane. *Hadamard transform optics*. Elsevier, 2012.

[16] FX Le Dimet J Ma. Deblurring from highly incomplete measurements for remote sensing. *IEEE Transactions on Geoscience and Remote Sensing*, 147(3):792–802, 2009.

[17] A. A. Michelson. On the application of interference methods to spectroscopic measurements. *The Philosophical Magazine*, 1891.

[18] Deanna Needell and Joel A Tropp. Cosamp: Iterative signal recovery from incomplete and inaccurate samples. *Applied and computational harmonic analysis*, 26(3):301–321, 2009.

[19] George R. Rossman. Mineral spectroscopy server. `http://minerals.gps.caltech.edu/index.html`, Oct 2016.

[20] D Siméoni, C Singer, and G Chalon. Infrared atmospheric sounding interferometer. *Acta Astronautica*, 40(2-8):113–118, 1997.

[21] Ming-Jie Sun, Matthew P. Edgar, David B. Phillips, Graham M. Gibson, and Miles J. Padgett. Improving the signal-to-noise ratio of single-pixel imaging using digital microscanning. *Opt. Express*, 24(10):10476–10485, May 2016.

[22] Dharmpal Takhar, Jason N. Laska, Michael B. Wakin, Marco F. Duarte, Dror Baron, Shriram Sarvotham, Kevin F. Kelly, and Richard G. Baraniuk. A new compressive imaging camera architecture using optical-domain compression. In *Proc. SPIE*, volume 6065, pages 606509–606509–10.

[23] T. Vasile, V. Damian, D. Coltuc, F. Garoi, and C. Udrea. Implementation of hadamard spectroscopy using moems as a coded aperture. *Proc. SPIE*, 9258:92581H–92581H–6, 2015.